

General framework for parameter optimization in imaging interferometric lithography

Eric S. Wu

University of New Mexico
Department of Electrical and Computer
Engineering
Albuquerque, New Mexico 87131-1356
E-mail: ericwu@ecece.unm.edu

Balu Santhanam

University of New Mexico
Department of Electrical and Computer
Engineering
Albuquerque, New Mexico 87131-1356
E-mail: bsanthan@ecece.unm.edu

S. R. J. Brueck

University of New Mexico
Department of Electrical and Computer
Engineering
Department of Physics and Astronomy
Albuquerque, New Mexico 87131
and
Center for High Technology Materials
University of New Mexico
Albuquerque, New Mexico 87106
E-mail: brueck@chtm.unm.edu

Abstract. Imaging interferometric lithography (IIL) employs the resolution enhancement technique (RET) of off-axis illumination (OAI) to overcome the spatial frequency resolution limitations that are imposed by the band limitedness of a conventional optical lithography system. IIL improves upon the aerial image resolution of a conventional optical lithography system by providing a wavelength division multiplexing approach toward the attainment of the maximum spatial frequency coverage of $2/\lambda$, which is independent of the numerical aperture of the optical system. IIL combines OAI, which provides access to higher spatial frequencies of the mask, with multiple exposures and several different configurations of the polarization parameters, the frequency parsing parameters, and the exposure energy ratios are possible. Although experiments detailing the resolution enhancement capabilities of IIL in isolated parameter settings exist, a unified approach toward parameter optimization in IIL that would enable automated software for TCAD is presently lacking. With the objective of providing a framework for parameter optimization in IIL, we propose in this paper, an approach that encompasses: (a) polarization diversity in the different on-axis or off-axis exposures of IIL, (b) an aggregate error metric for evaluating aerial image quality, (c) a block-based optimization process that incorporates the proposed error metric on representative, smaller blocks of the mask, (d) an optimization process that determines the optimal parameter settings for the entire mask using the lessons learned from the blocks. This framework for optimization of parameters in IIL enables comparison of IIL with other contemporary RETs and also enables the study and analysis of hybrid approaches such as combinations of IIL with optimal proximity correction. Simulation results that demonstrate the efficacy of the IIL-based approach and reinforce its capabilities as a viable RET for subwavelength optical lithography are presented. © 2005 Society of Photo-Optical Instrumentation Engineers. [DOI: 10.1117/1.1898246]

Subject terms: imaging interferometric lithography, optimization, frequency parsing, error metrics, catastrophic errors training sequence, polarization diversity, exposure energy ratios, and hybrid RET approaches.

Paper 03043 received Apr. 22, 2003; revised manuscript received Aug. 29, 2004; accepted for publication Dec. 20, 2004; published online Apr. 26, 2005.

1 Introduction

Imaging interferometric lithography (IIL) is a resolution enhancement technique (RET) that has been proposed for improving the resolution of aerial images produced by a conventional optical lithography system. Conventional optical lithography systems are constrained by the band limitedness of the underlying optics and unable to incorporate mask features containing higher spatial frequencies. IIL combines off-axis illumination (OAI) with multiple exposures to provide a wavelength division multiplexing approach toward attainment of the ultimate optical spatial frequency coverage of $2/\lambda$.¹ In its original configuration, due to the small numerical apertures (NA) used in the underlying optics, IIL needed to reintroduce a reference beam to ensure that the zero-order beam, i.e., the dc term of the mask is included back in the final imaging. The continuing advances in lens design and manufacturing however, cur-

rently capable of lenses with NA parameters of 0.9–0.95, have eliminated the need for the extra optics and consequently IIL can be treated as OAI with additional pupil plane filtering that ensures uniform weighting of the different spatial frequency components of the mask.

Prior work^{2–4} by Xiaolan Chen and co-workers has experimentally demonstrated the resolution enhancement capabilities of IIL, albeit at a low NA and for isolated configuration parameter settings. There are however, numerous possible combinations of experimental parameter settings in IIL that need to be determined and a framework for the optimization of these parameter settings has not yet been fully explored. Such a framework is needed to better understand the technical resolution limits of IIL, comparison of existing approaches, and for the investigation of other possible hybrid approaches that may yield more improvements in the resolution of the underlying aerial images.

In this paper, we propose a platform for parameter optimization in IIL, by first examining the pertinent equations

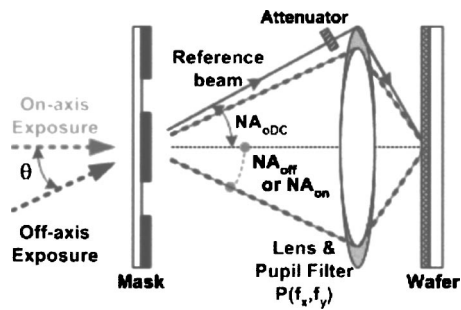


Fig. 1 Schematic for IIL setup, IIL off-axis exposure employs tilted coherent illumination with angle θ .

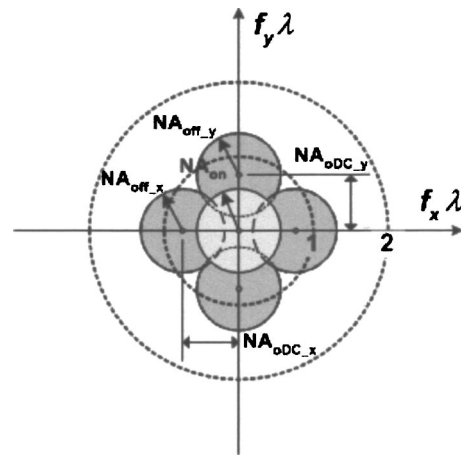


Fig. 2 Two-dimensional NA frequency parsing scheme for the different IIL exposures (the spatial frequency domain has been normalized with λ ; NA_{on} , NA_{off} are the pupil opening sizes for the IIL on-axis and off-axis exposures separately and NA_{odc} indicates the tilt angle in the off-axis illumination).

in IIL theory to understand factors such as the relative exposure energy ratios that play critical roles in the aerial image enhancement process. A detailed Fourier analysis of the IIL on-axis and off-axis exposures is presented using a scalar model to fully understand the essentials of constructing a high-resolution aerial intensity. This model specifically applies to the initial, around the lens reference-beam based, implementation of IIL. Then a vector-imaging model for two-dimensional (2-D) masks is applied to better explain polarization effects in aerial images and fully comprehend resolution improvements such as polarization diversity in the different exposures afforded by IIL. We then propose an optimization framework that includes an aggregate evaluative error function that combines several lithography-based error metrics to assess the quality of the aerial images produced and also eliminates undesirable solutions that result in the catastrophic errors by penalizing them heavily.

Optimization of the relevant configuration parameters is first performed on representative, smaller blocks of the

mask and a set of desirable parameter settings that constitute the training sequence are determined. This training sequence is used to initialize the optimization process on the entire mask. The proposed optimization framework will enable us to: (a) better understand the limitations and capabilities of this proposed IIL-based approach, (b) compare IIL with other approaches such as the partial coherent illumination method, (c) explore and analyze hybrid RET methods such as IIL-OPC that can provide further improvements in aerial image resolution.

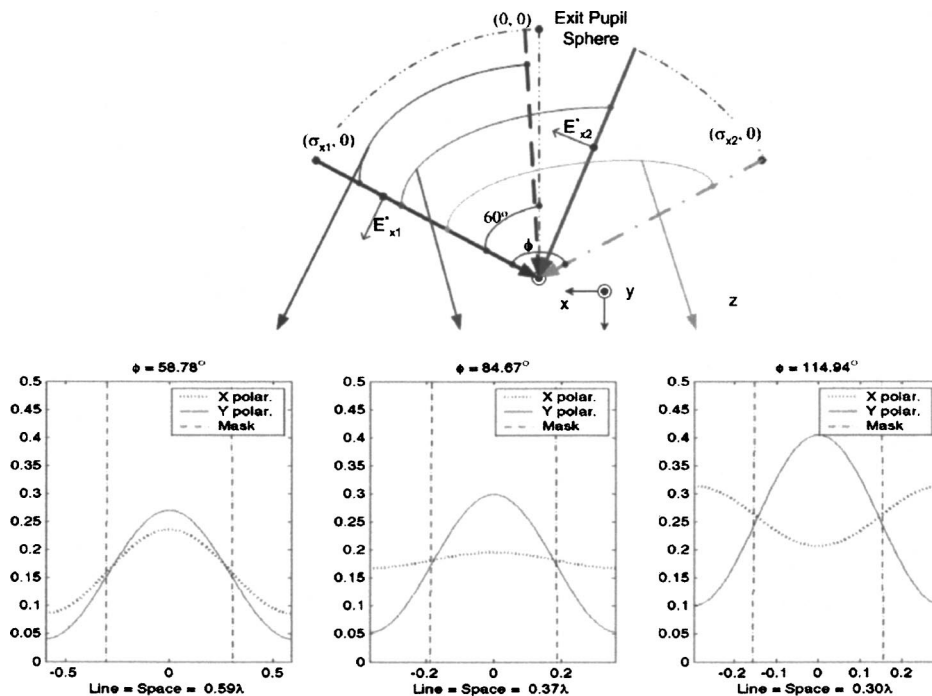


Fig. 3 Two-beam interference in the air with different incident angles (if the wrong light polarization is used, not only is the image contrast lost when ϕ is near 90° , but also the image is reversed when ϕ is larger than 90°).

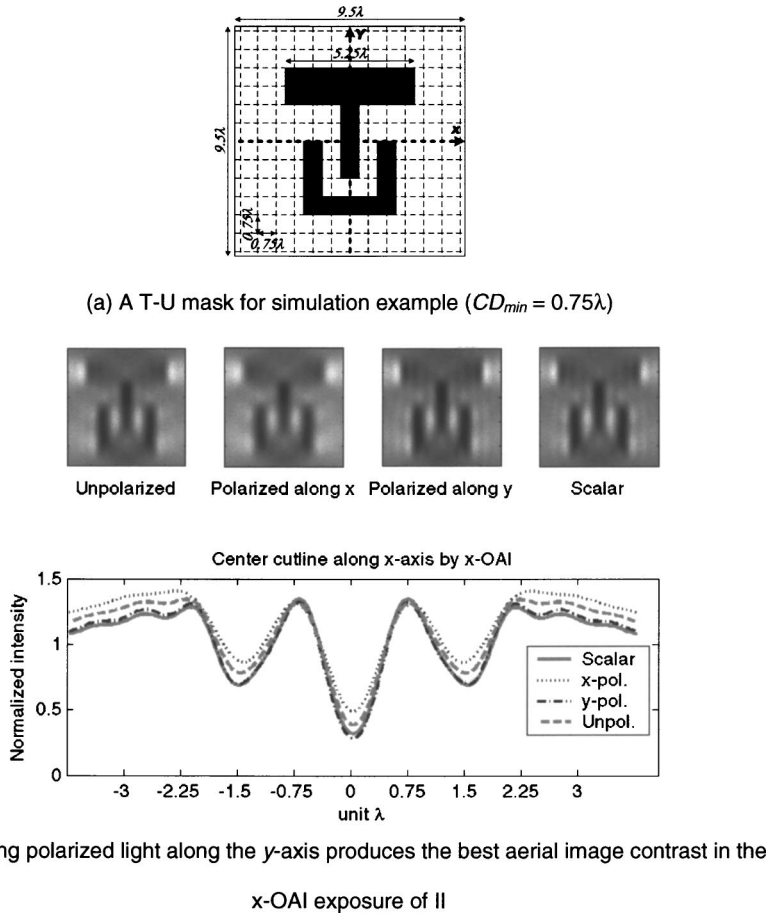


Fig. 4 IIL off-axis exposure along the x axis with different polarization configurations: (a) A T-U mask for simulation example ($CD_{min} = 0.75\lambda$) and (b) using polarized light along the y axis produces the best aerial image contrast in the x -OAI exposure of IIL.

2 Factors Affecting Aerial Image Formation

For Manhattan geometry, binary chrome masks, IIL configured as in Fig. 1 needs three different types of exposures: on-axis (I_{on}), off-axis along the x axis (I_{off_x}) and off-axis along the y axis (I_{off_y}). The resultant exposure energy from three different on-axis and off-axis IIL exposures can be expressed as

$$E_{IIL}(x,y) = \alpha I_{on}(x,y) + I_{off_x}(x,y) + I_{off_y}(x,y). \quad (1)$$

The first parameter α represents the energy ratio between IIL on-axis and off-axis exposures. A useful means of describing the resolution limits of IIL or, indeed, for any optical system is with spatial frequency analysis that corresponds to the 2-D spatial Fourier transform of the mask transmittance function. Figure 2 indicates the spatial frequency coverage of each IIL exposure in a frequency plot that is normalized by the illumination wavelength λ .

The frequency parsing scheme, i.e., the division of the spatial frequency space between different exposures among I_{on} , I_{off_x} and I_{off_y} can therefore be parameterized by NA_{on} , NA_{off_x} , and NA_{off_y} , which are the pupil opening sizes of the optical system for the IIL on- and off-axis exposures respectively. NA_{odc_x} and NA_{odc_y} are specifically indicative of the tilt angle θ in the off-axis illuminations along the x and y axes, where $\theta = \sin^{-1}(NA_{odc})$

$= \sin^{-1}(f_{odc}\lambda)$. From previous analysis with the scalar model,⁵ the resultant intensity in the Fourier domain with all three types of exposures is given as

$$\begin{aligned} \mathbf{F}\{I_{IIL}(x,y)\} = & \alpha \cdot \mathbf{F}\{I_{on}(x,y)\} + 2\{\gamma_x^2 \delta(f_x, f_y)\} \\ & + 2\{E_{off_x}(f_x + f_{odc}, f_y) \otimes E_{off_x}^*(-f_x \\ & + f_{odc}, f_y)\} + 2\gamma_x\{E_{off_x}(f_x, f_y) \\ & + E_{off_x}^*(-f_x, f_y)\} + 2\{\gamma_y^2 \delta(f_x, f_y)\} \\ & + 2\{E_{off_y}(f_x, f_y + f_{odc}) \otimes E_{off_y}^*(f_x, -f_y \\ & + f_{odc})\} + 2\gamma_y\{E_{off_y}(f_x, f_y) \\ & + E_{off_y}^*(-f_x, f_y)\}, \end{aligned} \quad (2)$$

where γ_x^2 and γ_y^2 are parameters referring to the initial off-axis illumination exposure energies. Assuming that the in-lens imaging pupil transmission functions $P_{off_x}(f_x, f_y)$ and $P_{off_y}(f_x, f_y)$ are circular low-pass cutoff filters with pupil size of NA_{off_x} and NA_{off_y} , respectively, E_{off_x} and E_{off_y} can then be deemed as high spatial frequency portions of the mask's transmittance function $T(f_x, f_y)$:

$$E_{off_x}(f_x, f_y) = T(f_x, f_y) P_{off_x}(f_x - f_{odc_x}, f_y),$$

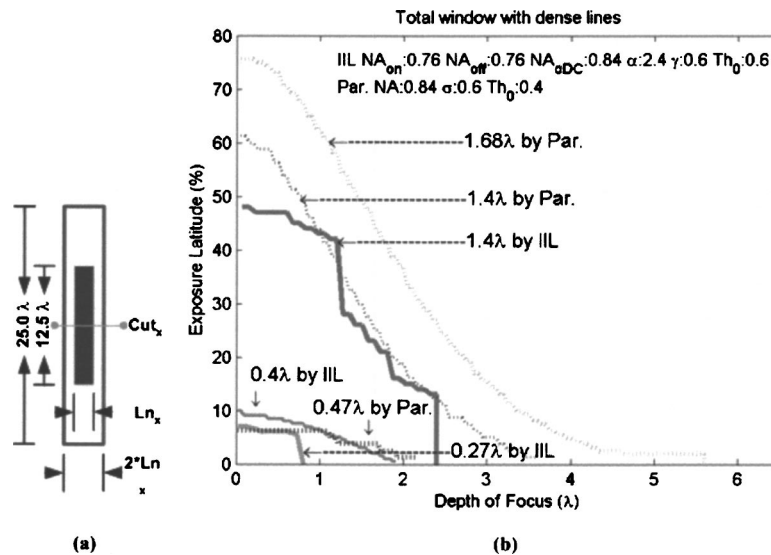


Fig. 5 Total window for IIL and partial-coherent illumination scheme (IIL with the printed linewidth=0.4λ had the almost same process latitude that using the partial coherent illumination with the printed linewidth=0.47λ).

$$E_{\text{off}_y}(f_x, f_y) = T(f_x, f_y) P_{\text{off}_y}(f_x, f_y - f_{\text{odc}_y}). \quad (3)$$

These results indicate that IIL is able to recover the mask information back in a linear fashion with retro-parameters (γ_x, γ_y) and with additional nonlinear terms that may induce lithographic errors that need to be corrected by an optimization procedure. For the discussions presented in this paper, in the interest of brevity, we will restrict the set of parameters that need to be optimized to the relative exposure energy parameters by fixing the frequency coverage parameters. We also restrict the mode of illumination in the IIL exposures to conventional coherent illumination. (Large frequency offsets needed for extreme OAI can only be achieved with a coherent illumination source with a very small partial coherence.⁴ Further, quadrupole illumination is the preferred mode of illumination for Manhattan geometry patterns.⁴)

3 Polarization Effects and Polarization Diversity at High NA

In high-NA imaging systems, especially those currently used in the OAI and IIL methods, judicious application of an appropriately polarized light source prevents the loss of aerial image contrast. For example, two-wave interference in air is described in Fig. 3 by the zero- and first-order beam from a dense line-grating mask along the y axis. The reference beam (the zero-order) is fixed at an angle $\sim 60^\circ$ with respect to the axis of illumination and the intensities from the individual two beams are adjusted to the same. From the results with angle $\phi = 58.78^\circ, 84.67^\circ, \text{ and } 114.94^\circ$ between two plane waves, the aerial images not only show that the aerial image contrast produced by E_x^* (polarized light with an initial electric field vector along the x axis, asterisk denotes complex conjugation) will be less than that with E_y^* , but also indicate that a very large angle $\phi > 90^\circ$ would cause printed patterns to be shifted in such a manner that may increase the risk of producing errors with 2-D masks.

Since these polarization effects become critically important for high NA systems, in this paper we implemented aerial image modeling as the weighted sum of propagating plane waves⁶ incorporating the correction factors given by Mansuripur⁷ for the modeling formula.⁸ The example described in Fig. 4 is generated with this vector-imaging model and is specifically for the intrinsic high-NA characteristics of IIL produced by the reference beam ($\text{NA}_{\text{odc}} = 0.84$ in the example). A T-U mask with $\text{CD}_{\text{min}} = 0.75\lambda$ in wafer scale is shown in Fig. 4(a) and the mask simulations are obtained by setting a $4\times$ reduction stepper with $\text{NA}_{\text{on}} = 0.76$, $\text{NA}_{\text{off}_x} = \text{NA}_{\text{off}_y} = 0.76$, $\text{NA}_{\text{odc}_x} = \text{NA}_{\text{odc}_y} = 0.84$ and γ_x, γ_y for the reference beam are set to one. In Fig. 4(b), $I_{\text{off}_x}(x, y)$ are generated by different IIL off-axis exposure along the x axis with different polarization configurations and the Fourier scalar model. Clearly using light that is polarized along the y -axis produces the best contrast. On the other hand with $I_{\text{off}_y}(x, y)$, i.e., the IIL off-axis exposure along the y axis, light that is polarized along the x axis produces the best contrast results. Since IIL incorporates multiple exposures, we are able to use differently polarized light for different off-axis illumination angles, i.e., incorporate polarization diversity to improve aerial image resolution, where other related OAI based methods are unable to do so.

Figure 5 shows the total window analysis⁹ of dense 2-D grating lines. Based on the vector-imaging model, we ran simulations using different sizes of 2-D block masks in Fig. 5(a) using a constant threshold resist (CTR) development model¹⁰ with a threshold parameter Th_0 that is related to the normalized exposure dosage. Under the same mask with the grating linewidth=1.56λ in the x direction, IIL produced a 1.4λ line while partial-coherent illumination method produced a 1.68λ line. With the partial-coherent illumination scheme, patterns in the mask tend to become smoothed and spread out in printed patterns on the wafer. Consequently, we conclude that subresolution feature insertion in the OPC technique is more difficult with partial-

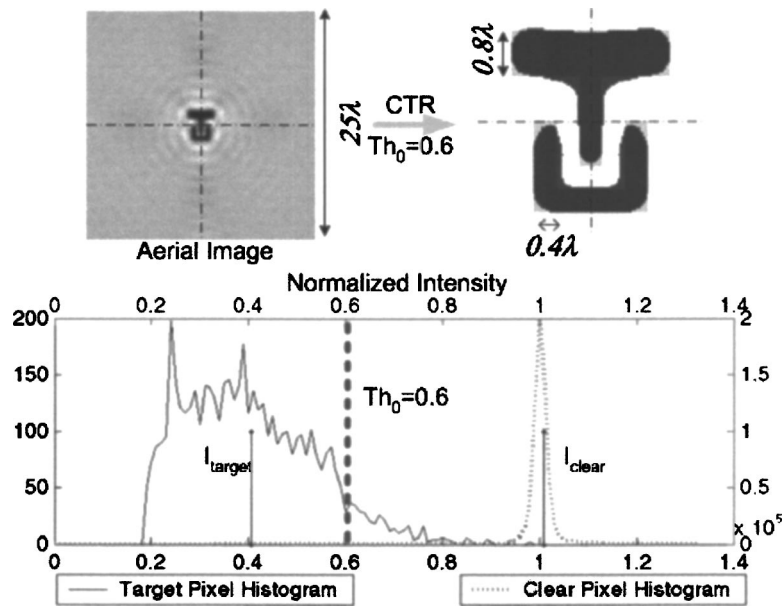


Fig. 6 Placement error measure (PEM) and aerial contrast error measure (ACE). (At the upper-right corner, PEM is computed by counting the number of pixels that are in error between printed and target patterns after the CTR model. At the bottom, a wider histogram gap between I_{target} and I_{clear} indicates better aerial image contrast.)

coherent illumination than with IIL due to the lesser degree of freedom available for using gaps between patterns. Because the reference beam in the IIL off-axis exposure in our example is arriving at a large incident angle upon the wafer, the large phase differences introduced by defocus effects such as lens aberrations or curvature could produce a smaller depth of focus in IIL in comparison to the partial coherent illumination scheme when printing large patterns such as the one with a printed linewidth = 1.4λ described in Fig. 5. For features in the subwavelength regime, and with the aerial image enhancement (higher visibility), IIL still retains acceptable process latitude in comparison to the partial-coherent illumination method because high-order beams are arriving from a direction different from the reference beam and consequently there is lesser phase difference that may result in defocus effects. In Fig. 5, the exposure latitude with IIL in the printed linewidth = 0.4λ case was better than that obtained with the partial-coherent illumination method in the printed linewidth = 0.47λ case. Through simulations using 2-D gratings of different sizes, the minimum printable CD in our IIL example reached 0.27λ , which is much better than 0.47λ accessible with the partial-coherent imaging scheme with $\sigma=0.6$.

4 Assessment of Aerial Image Quality: An Aggregate Error Metric

Before describing the parameter optimization process, criteria for distinguishing good and bad aerial images from each other or more generally a performance metric for the assessment of aerial image quality are needed. Global assessment guidelines such as the mean squared error metric that consider the whole mask/chip are not suitable for lithography applications because many of the aerial image imperfections such as edge defects are localized and would be averaged out when considering the entire mask. We specifically desire that those solutions that result in cata-

strophic defects and eventual failure in the underlying printed circuit be penalized heavily. (Island, pinhole, bridge, and break errors in the top-down profile constitute the possible catastrophic errors and will result in circuit failure or leakage currents in the resultant circuits.) Several localized error metrologies such as the MEEF¹¹ and the exposure-defocus windows¹² have been proposed for optimization in lithography specifically for line structures. In addition, most approaches towards defining lithographic error metrics for optimization purposes are pattern specific and employ methods that involve explicit tagging of the 2-D masks in order to know where to look or measure.

These measures could be placement error measure (PEM), line-end shortening (LES), and corner rounding error (CRE). Hence, we propose the use of an aggregate error measure on the top-down view that is highly correlated with the quality of the corresponding aerial images or resist profiles. Since high quality photoresist materials with low absorption and high contrast properties are available, the exposure dose through resist depth is usually uniform and can produce high fidelity patterns with steep sidewalls. Consequently one can directly connect the quality of the aerial image profiles to resist profiles by using the CTR model.

Quantifying aerial image contrast quality through histogram plots is a useful optimization tool, where the histograms are used to show the pixel distribution of intensity levels. Let us look at the histogram plots in Fig. 6 that are comprised of two groups of histograms and they are denoted as "Target Pixel Histogram" and "Clear Pixel Histogram." These two histograms are created by overlapping the normalized aerial image pixels with the corresponding target patterns, where "target pixels" are for the regions that should have resist remains and "clear pixels" are for those that should be cleared. The PEM error metric can then be calculated by counting the number of clear pixels with in-

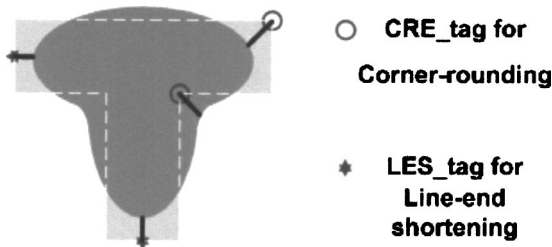


Fig. 7 Edge analyses on the top-down profile.

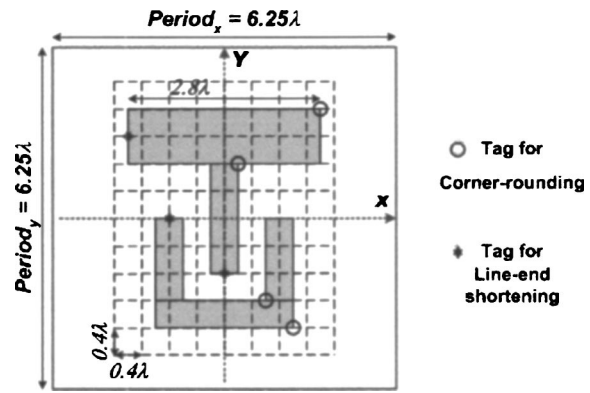


Fig. 8 Target template for the example T-U.

tensities that are lower than Th_0 and target pixels with intensities that are higher than Th_0 , where Th_0 is the threshold parameter from the CTR model. To quantify and evaluate the 2-D aerial image contrast quality as in Fig. 6, we can use the average intensity of clear pixels I_{clear} and the average intensity of target pixels I_{target} . Specifically the intensity difference between these two averages provides useful information on the overall image contrast. To express this contrast quality in the error form, the aerial contrast error (ACE) metric for positive resist is defined as

$$ACE = 1 - (I_{clear} - I_{target}). \quad (4)$$

Combing this metric and other error measures described in Fig. 7,

$$PEM(\%) = \frac{[\text{pixels (overlay difference between printed and target patterns)}/\text{pixels (target patterns)}], \quad (5)$$

$$LES = \frac{[|\text{pixel}_{\text{printed_edge}}(x,y) - \text{pixel}_{\text{LES_tag}}(x_0,y_0)|_{\text{along the } x \text{ or } y \text{ axis}}/\text{pixel counts of } CD_{\min}], \quad (6)$$

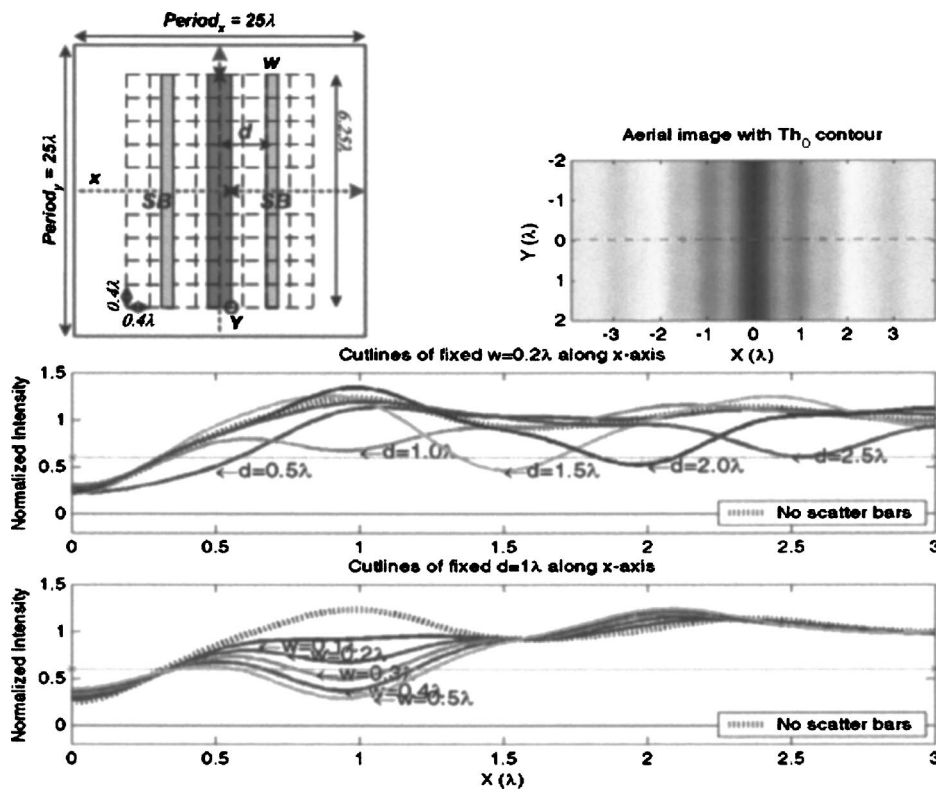


Fig. 9 Scattering bar configuration for OPE (bottom panel depicts the changing of the x-axis cutline intensity for various w and d parameters) mask.

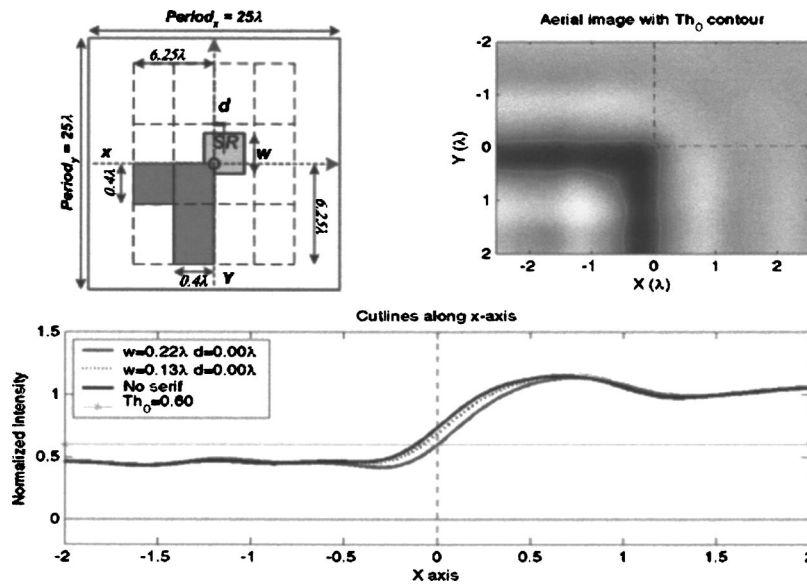


Fig. 10 Dark serif configuration for corner rounding (bottom panel depicts the change in the x-axis cutline intensity).

$$\begin{aligned}
 \text{CRE} = & \left[\left| \text{pixel}_{\text{printed_edge}}(x,y) \right. \right. \\
 & \left. \left. - \text{pixel}_{\text{CRE_tag}}(x_1,y_1) \right|_{\text{along the } 45^\circ \text{ or } 135^\circ \text{ line}} / \text{pixel} \right. \\
 & \left. \text{counts of } \text{CD}_{\text{min}} \right]. \tag{7}
 \end{aligned}$$

Note that the expressions for the edge-based metrics of LES and CRE are identical apart from points or tags on the mask where these measurements are made. We propose collecting bits and pieces of information from critical locations between target and printed patterns, and organizing these measures such as PEM, LES, and CRE in such a manner that makes quality assessment more objective and suitable to software automation in TCAD. After the aerial intensity image passes the most important stage of catastrophic error checking in our optimization procedure, a cumulative error measure (CEM) for imaging performance is used for qualifying printed patterns and formulated with error measure procedures from Eqs. (4)–(7) as

$$\begin{aligned}
 \text{CEM}(z) = & e_1 \text{PEM}(z) + e_2 \text{ACE}(z) + e_3 \text{avg}\{\text{LES}(z)\} \\
 & + e_4 \text{avg}\{\text{CRE}(z)\}, \tag{8}
 \end{aligned}$$

where z is the defocus distance from the best focus and e_i are the weightings for each individual error measure.

The numbers from these error measures are mask dependent and are also dependent on the measuring positions (tags) at the target template, consequently the ability to choose/manipulate the relative weightings e_i in the CEM equation [Eq. (8)] so that differences numerically between good and had printed resist patterns are better emphasized, will depend on the training sequence that we choose for this purpose. A training sequence (this terminology is borrowed from the neural networks arena, where a statistically representative training sequence is first used to enable the network to learn information regarding the signal environment before being applied on real data) by definition contains several candidate printed patterns that have been sorted in terms of quality from the best to the worst by experienced

lithography engineers. For example, with a target template described in Fig. 8 there are three tags for LES and four tags for CRE measurement locations. We generate the printed patterns that correspond to the training sequence by randomly choosing different exposure energy ratios (α , γ_x , and γ_y) in the IIL imaging scheme, the individual error numbers are then tabulated for each result. In order to match the priority of the training sequence member that we prefer, the relative weighting values e_i in Eq. (8) are chosen manually and carefully as $[e_1, e_2, e_3, e_4] = [1, 14, 6, 250]$ so that we can order the computed $\text{CEM}(z=0)$ values for the different printed results from the smallest to the largest in accordance with priority. The weighting values e_i usually vary with different target templates, where usually PEM is the dominating factor in the aggregate error function. However, since corner rounding in this T–U mask example is the major concern, e_4 for CRE is given a heavier weighting than other error measures.

5 Hybrid Approaches: IIL-OPC Study

In the proposed IIL scheme, due to the presence of different linewidths and the underlying dense-iso bias problem associated with the mask features, the transition of a spatial frequency component associated with the mask from the on-axis exposure to an off-axis exposure means that the MEEF and optical proximity effect (OPE) performance curves have sharp transitions unlike the smooth curves found with the partial-coherent illumination method.⁹ In addition to using judicious feature placement on the mask through thoughtful analysis of the spatial frequency content of the features and application of different frequency-parsing strategies, we could avoid the jumps seen in the MEEF/OPE curves from occurring in the frequency ranges that the desired pattern occupies by applying OPC techniques. We can then prevent the occurrence of catastrophic errors in the resulting aerial image by penalizing those solutions that result in these catastrophic errors heavily. Fur-

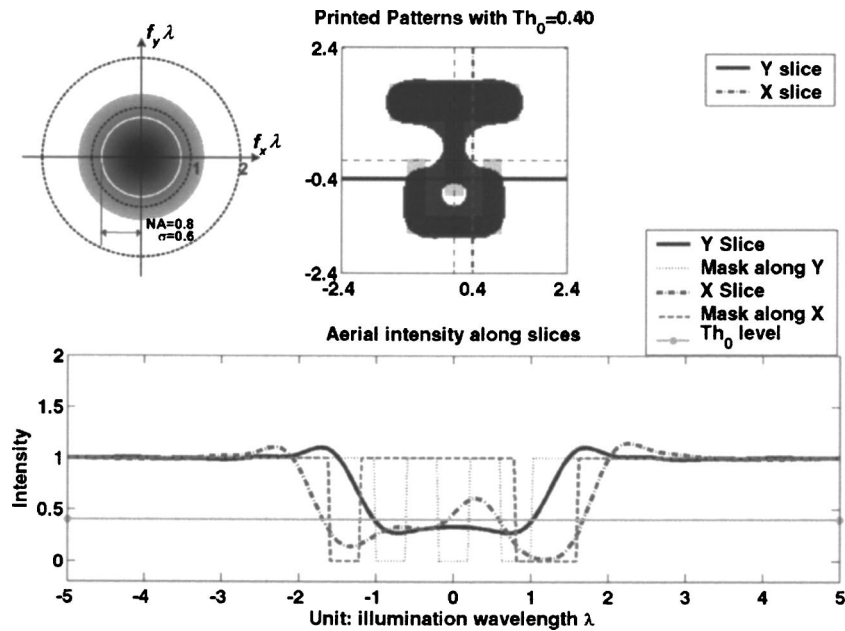


Fig. 11 T-U mask with the partial-coherent illumination (dense feature region is not resolved due to $CD_{min}=0.47\lambda$ and a low image contrast).

ther, the lithographic edge-quality errors such as LES and CRE can simultaneously be minimized easily with model-based OPC approaches.

The main purpose of employing additional scattering bars (SB)¹³ as shown in Fig. 9 at $1\times$ wafer scale is to reduce the OPE difference between isolated lines and dense lines. This approach has been shown to improve CD targeting and DOF.¹⁴ The modeling configuration for applying SB OPC is parameterized by a pair of factors: (a) width of the SB (w) and (b) the SB separation distance (d) to the main feature. They are described and clearly indicated at the upper-left corner of Fig. 9. Through simulations on various widths and displacements of the scattering bars, the optimization procedure for IIL OPC SB computes the error measures on the resultant patterns. The illustration describing the changing of the x -axis cutline intensity of aerial images is shown at the bottom of Fig. 9. With a main linewidth= 0.5λ , the behavior of IIL is different from that of the partial-coherent imaging¹⁵ method. Even for a large distance parameter $d=2\lambda$, a wrong displacement of the subresolution SB with width parameter $w=0.2\lambda$ with IIL could induce additional printable results such as *ghost lines* that are forbidden in any circumstance and in our example with $d=\lambda$, the width parameter w should be less than 0.2λ .

To investigate another possible OPC-based hybrid approach, square serifs are introduced at the corners of line-turn and line-end as shown in Fig. 10 for a dark serif. Similar to SB, two parameters are used in the SR configuration modeling, w for the size of the SR square and d for the distance from the center of the SR square to the axes while moving the serif diagonally along 45° . To demonstrate that OPC serif is applicable in IIL, after modeling the effects of the serif size and placement in IIL OPC, we measure the CRE from the printed results for a linewidth= 0.4λ corner of the mask. The best placement for a dark serif is $d=0$ and $w=0.22\lambda$, whereas the size and placement pair $d=0.06\lambda$ and $w=0.53\lambda$ works best for a clear serif under





the IIL parameter configuration of $(\alpha, \gamma_x, \gamma_y, Th_0) = (2.4, 0.6, 0.6, 0.6)$.

Upon completing the description of the optimization framework, we can now use this framework to evaluate the limitations, and more generally the performance of IIL and related hybrid approaches with other contemporary resolution enhancement techniques such as the partial coherent illumination method. Application of apodized pupil filtering in each exposure with raised cosine filters can also be used to smoothen the transition from on-axis exposure to off-axis exposure, can further alleviate the abruptness in the IIL MEEF/OPE curves, and can also help in improving aerial image contrast.¹⁶

6 Measures on IIL Performance with a 2-D Manhattan Mask

With the vector-imaging model, and using the T-U mask/target pattern described in Fig. 8, setting $CD_{min}=0.4\lambda$, and the overall size of the simulation region $period_x=period_y=25\lambda$, the printed results of the partial-coherent illumination approach ($NA=0.84$ and $\sigma=0.6$) are shown in Fig. 11. From the previously described ED window analysis, we concluded that the minimum printable linewidth is only 0.47λ with the partial-coherent illumination scheme and catastrophic errors (bridges) appear between the dense lines (0.4λ) in Fig. 11. Due to the lack of aerial image contrast that is depicted in the aerial image intensity plots at the bottom of the figures, independent of the adjustment that we use for the threshold parameter Th_0 of the CTR model, there will always exist catastrophic errors in the examples. As for IIL, the configuration that was used was without any pupil filtering and the IIL optical system configuration was $NA_{on}=0.76$, $NA_{off,x}=NA_{off,y}=0.76$ and $NA_{odc,x}=NA_{odc,y}=0.84$. We used: (a) unpolarized coherent light

Table 1 Optimization results for T-U mask [the order of the second row is $(\alpha, \gamma_x, \gamma_y, Th_0)$ and the best result is (2.0,0.8,0.8,0.6)].

	Priority 1		Priority 2
	(2.0, 0.8, 0.8, 0.6)		(1.2, 0.6, 0.6, 0.6)
	CEM 101.56		CEM 101.88
	PEM 20.502		PEM 21.495
	ACE 0.44634		ACE 0.42081
LES 0.26042	LES 0.20833		
CRE 0.29297	CRE 0.29297		
	Priority 3		Priority 4
	(2.0, 0.8, 0.6, 0.6)		(2.8, 0.8, 1.0, 0.6)
	CEM 102.33		CEM 102.69
	PEM 19.841		PEM 21.144
	ACE 0.41345		ACE 0.45092
LES 0.16927	LES 0.33203		
CRE 0.30273	CRE 0.29297		

for I_{on} , polarized light along the y axis for I_{off_x} and (b) polarized light along the x axis for I_{off_y} (incorporated polarization diversity).

The block optimization procedure⁸ with the aggregate error function defined in Eq. (8) is then applied to representative blocks of the mask with relative weightings factors of $[e_1, e_2, e_3, e_4] = [1, 10, 3, 3]$ and is computed at the best focus, i.e., $CEM(z=0)$ and at the defocus plane, i.e., $CEM(z=0.5\lambda)$ in hundreds of simulations. Then from these numerous computed solutions we pick the best 81 possible solutions which constitute the training sequence; we then ran the optimization process on the whole mask by using another set of weightings $[e_1, e_2, e_3, e_4] = [1, 14, 6, 250]$ for the T-U mask. The top four resultant choices from the optimization process on the entire mask pattern are listed in Table 1, where the information on the exposure energy ratios and the threshold parameter are given in the order of $(\alpha, \gamma_x, \gamma_y, Th_0)$ and the computed error measures were the average values obtained from the best focus ($z=0$) and the defocus plane ($z=0.5\lambda$). Finally, we chose the suboptimal¹⁷ set of values for the exposure

energy ratios and threshold as: $(\alpha=2.0, \gamma_x=0.8, \gamma_y=0.8, Th_0=0.6)$ and the corresponding printed result is shown in Fig. 12. Clearly, in addition to eliminating the parameters that correspond to IIL configurations that result in catastrophic errors, the results of optimizing the exposure energies serves to illustrate that parameter optimization can significantly improve the resolution of aerial images even in situations where the partial-coherent illumination scheme fails.

If further resolution improvements at the line ends and corners are required, then the hybrid approach that combines IIL with model-based OPC, i.e., IIL-OPC that was discussed in the previous section is applied. The resultant OPC masks and the corresponding printed pattern outcomes are shown in Fig. 13 and the specific error measurements before OPC and after the application of OPC are listed in Table 2. They indicate an improvement in the resolution of the underlying aerial images of the hybrid scheme, IIL OPC, over just IIL.

7 Conclusions and Future Research Directions

In this paper, we have presented a novel framework for optimization of some specific IIL configuration parameters such as the relative exposure dosages, polarization diversity of light in the individual IIL exposures, and the threshold parameter in the CTR model. The proposed optimization process incorporates an aggregate lithographic error metric for assessing both the quality of the aerial images produced and for determining acceptable solutions for these parameters specifically applied to representative blocks of the mask. The set of these desirable candidates termed the training sequence is then used to initialize the optimization process on the entire mask. This optimization process, akin to training and optimization using neural networks, with polarization diversity incorporated into the different IIL exposures was shown to produce significant improvement in

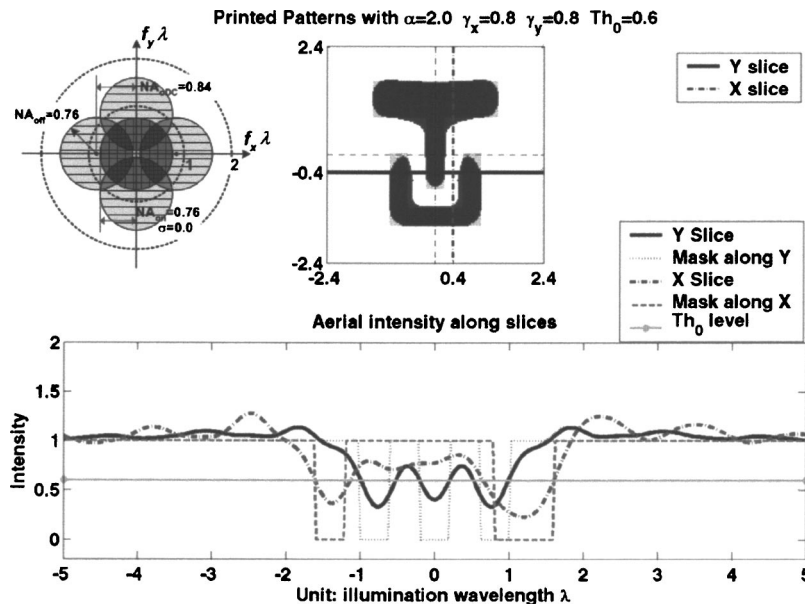


Fig. 12 T-U mask with IIL after the energy optimization (patterns are printed without catastrophic errors).

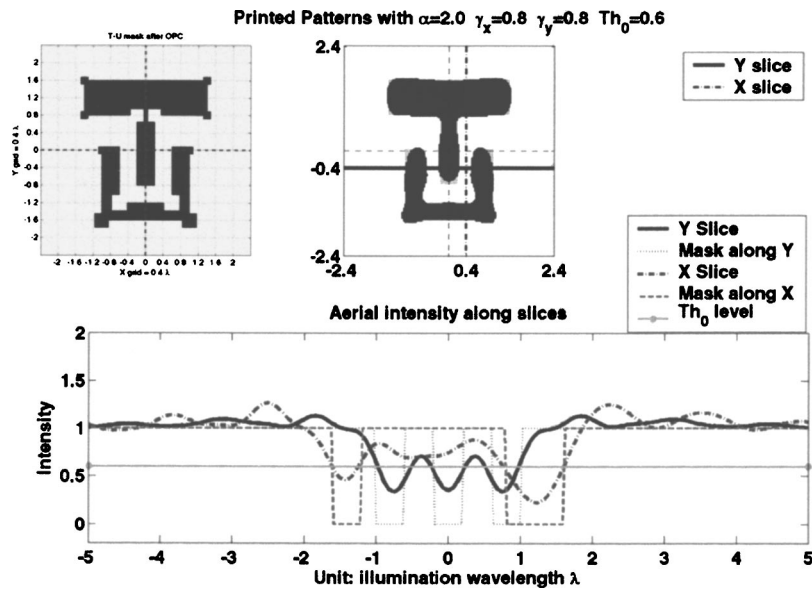


Fig. 13 T-U mask with IIL after the OPC procedure (serifs are applied for corner rounding).

aerial image resolution over the partial coherent illumination scheme, while simultaneously eliminating solutions that resulted in catastrophic errors.

We further investigated hybrid approaches like IIL OPC to further improve aerial image resolution, where OPC was used to smooth jumps in the MEEF/OPE curves that are produced when a spatial frequency component of the mask moves from the on-axis exposure to the off-axis exposure. The simulations presented in this paper, specifically the IIL 2-D mask example with polarization diversity, resulted in a minimum resolvable feature size of $CD_{min}=0.4\lambda$ (77 at 193 nm) and demonstrate the efficacy/viability of this IIL-based approach toward subwavelength optical lithography. Future research directions that are currently being investigated are: (a) incorporating the optimization of the critical spatial frequency coverage parameters¹⁶ into a multistage optimization framework (optimization of the frequency coverage parameters is a separate combinatorial optimization problem over the different possible spatial frequency sets and the different IIL exposures; joint optimization of coverage parameters with the relative exposure energies, albeit a more optimal framework, would make the overall optimization problem non tractable), (b) incorporation of apodized pupil filters¹⁶ into this optimization framework, where this has been shown to further improve aerial image contrast, (d) study of other hybrid approaches such as IIL PSM. These hybrid approaches along with the optimization framework have the potential for providing further im-

provement in aerial image resolution, reduction in minimum printed feature size. This claim is consistent with the notion envisaged in recent literature that looks at trends in applied optics¹⁵ that “theoretically there are no fundamental limits to optical lithography,” and what remains to be seen is whether these approaches are economically viable.

Acknowledgments

This work was done in collaboration with the Center for High Technology Materials (CHTM), University of New Mexico, Albuquerque and was supported by an ARO/MURI (Grant No. DAAD19-99-1-0196): Deep Subwavelength Optical Nanolithography.

References

1. S. R. J. Brueck, “Imaging interferometry—a novel approach to nm-scale optical lithography,” *Microlithogr. World* **7**(1), 2–10 (1998).
2. X. Chen, “A study of interferometric lithography—approaching the linear system limits of optics,” PhD thesis, University of New Mexico (1998).
3. X. Chen and S. R. J. Brueck, “Imaging interferometric lithography: a wavelength division multiplex approach to extending optical lithography,” *J. Vac. Sci. Technol. B* **16**(6), 3392–3397 (1998).
4. X. Chen and S. R. J. Brueck, “Experimental comparison of off-axis and imaging interferometric lithography,” *J. Vac. Sci. Technol. B* **17**(3), 921–929 (1999).
5. E. S. Wu, B. Santhanam, and S. R. J. Brueck, “Grating analysis of frequency parsing strategies for imaging interferometric lithography,” *Proc. SPIE* **5040**, 1276–1283 (2003).
6. M. S. Yeung, “Modeling high numerical aperture optical lithography,” *Proc. SPIE* **2726**, 149–167 (1988).
7. M. Mansuripur, “Distribution of light at near the focus of high-numerical-aperture objectives,” *J. Opt. Soc. Am. A* **10**, 382–388 (1993).
8. D. G. Flagello and T. D. Milster, “High-numerical-aperture effects in photoresist,” *Appl. Opt.* **36**(34), 8944–8951 (1997).
9. A. K. Wong, *Resolution Enhancement Techniques in Optical Lithography*, pp. 66–68, SPIE Press, Bellingham, Washington (2001).
10. T. A. Brunner and R. A. Ferguson, “Approximate models for resist processing effects,” *Proc. SPIE* **2726**, 198–207 (1996).
11. F. M. Schellenberg and C. A. Mack, “MEEF in theory and practice,” *Proc. SPIE* **3873**, 189–202 (1999).
12. B. J. Lin, “The exposure-defocus forest,” *Jpn. J. Appl. Phys., Part 1* **33**(12B), 6756 (1994).
13. J. F. Chen, T. Laidig, K. E. Wampler, R. Caldwell, K. H. Nakagawa, and A. Liebchen, “A practical technology path to sub-0.10 micro

Table 2 Error measurements on printed patterns before and after the application of model-based OPC.

OPC	T-U mask			
	PEM	ACE	LES	CRE
Before	17.1629	0.3977	0.2344	0.3125
After	13.1307	0.4184	0.1172	0.1172

- process generations via enhanced optical lithography," *Proc. SPIE* **3873**, 995–1016 (1999).
14. J. F. Chen, T. Laidig, K. E. Wampler, and R. Caldwell, "Practical method for full-chip optical proximity correction," *Proc. SPIE* **3051**, 790–803 (1997).
 15. K. Adam and A. Neureuther, "Analysis of OPC features in binary masks at 193 nm," *Proc. SPIE* **4000**, 711–722 (2000).
 16. S. R. J. Brueck, *There are no Fundamental Limits to Optical Lithography: International Trends in Applied Optics*, A. Guenther, Ed., pp. 85–110, SPIE Press, Bellingham, Washington (2002).
 17. T. M. Tridhavec, B. Santhanam, and S. R. J. Brueck, "Optimization and apodization of aerial images at high NA in imaging interferometric lithography," *Proc. SPIE* **5377**, 1544–1554 (2004).

Eric S. Wu received his BS degree in electronics engineering from National Chiao Tung University, Taiwan in 1992. After a two-year military service and receiving his MS degree in electrical engineering from University of Southern California in 1996, he joined Trident Microsystems, based in Sunnyvale, California, as a circuit designer for two years. He received his PhD in electrical engineering in 2003, at University of New Mexico. His research interests include modeling, parameter optimization, and TCAD for imaging interferometric lithography.

Balu Santhanam received his BS degree in electrical engineering from St. Louis University, St. Louis, Missouri, in 1992. He obtained his MS and PhD degrees in electrical engineering from the Georgia Institute of Technology, Atlanta, in 1994 and 1998, respectively. From 1998 to 1999, he was a lecturer and postdoctoral researcher with the Department of Electrical and Computer Engineering at the

University of California, Davis. In 1999, he joined the faculty of the Department of Electrical and Computer Engineering at the University of New Mexico, Albuquerque, where he is presently an Assistant Professor. He currently serves as the associate editor for the International Journal on Computer and Electrical Engineering, Elsevier Science. His current research interests include multiple access interference reduction in CDMA systems, multicomponent AM–FM signal separation, modulation/demodulation, and time–frequency representations for nonstationary signals, imaging interferometric lithography and IIL-related parameter optimization for subwavelength optical lithography. He is a member of the SPIE, the signal processing and communication societies of the IEEE, and a member of the ASEE.

S. R. J. Brueck received his BSc from Columbia University in 1965 and his MSc/PhD from MIT in 1967/1971. In 1971, he joined the Quantum Electronics Group at MIT Lincoln Laboratory. In 1985, he became the director of the Center for High Technology Materials (CHTM) and a professor of electrical and computer engineering and physics at the University of New Mexico. He has extensive experimental and theoretical research contributions to many aspects of optics and laser spectroscopy. Material systems investigated include semiconductors, simple molecular liquids, and plasmas used for semiconductor processing. Under his direction, CHTM has become an internationally recognized center for optoelectronics and microelectronics related research. He has over 200 published research articles, has edited 7 books, been awarded 21 patents, and serves as editor of several journals. He is a fellow of the IEEE and OSA societies and recipient of the IEEE Third Millennium Award.